

Photoelectric absorption cross section of silicon near the band gap from room temperature to sub-Kelvin temperature

C. Stanford,^{1, 2, a)} M.J. Wilson,^{3, 4} B. Cabrera,^{1, 5, b)} M. Diamond,³ N.A. Kurinsky,^{6, 7} R.A. Moffatt,¹ F. Ponce,¹ B. von Krosigk,⁴ and B.A. Young⁸

¹⁾ *Department of Physics, Stanford University, Stanford, CA 94305 USA*

²⁾ *Department of Physics, Harvard University, Cambridge, MA 02138 USA*

³⁾ *Department of Physics, University of Toronto, Toronto, ON M5S 1A7, Canada*

⁴⁾ *Institut für Experimentalphysik, Universität Hamburg, 22761 Hamburg, Germany*

⁵⁾ *SLAC National Accelerator Laboratory/Kavli Institute for Particle Astrophysics and Cosmology, 2575 Sand Hill Road, Menlo Park, CA 94025 USA*

⁶⁾ *Fermi National Accelerator Laboratory, Center for Particle Astrophysics, Batavia, IL 60510 USA*

⁷⁾ *Kavli Institute for Cosmological Physics, University of Chicago, Chicago, IL 60637, USA*

⁸⁾ *Department of Physics, Santa Clara University, Santa Clara, CA 95053 USA*

(Dated: 2 November 2020)

The use of cryogenic silicon as a detector medium for dark matter searches is gaining popularity. Many of these searches are highly dependent on the value of the photoelectric absorption cross section of silicon at low temperatures, particularly near the silicon band gap energy, where the searches are most sensitive to low mass dark matter candidates. While such cross section data has been lacking from the literature, previous dark matter search experiments have attempted to estimate this parameter by extrapolating it from higher temperature data. However, discrepancies in the high temperature data have led to order-of-magnitude differences in the extrapolations. In this paper, we resolve these discrepancies by using a novel technique to make a direct, low temperature measurement of the photoelectric absorption cross section of silicon at energies near the band gap (1.2–2.8 eV).

I. INTRODUCTION

The photoelectric absorption cross section ($\sigma_{\text{p.e.}}$) of silicon at low temperatures is an important parameter for modern experiments that use cryogenic silicon as a substrate for the direct detection of dark matter^{1–5}. Several dark matter signal models depend on this parameter. We discuss these models in more detail in von Krosigk *et al.*⁶, but will highlight two of them here.

First, the hypothesized kinetic mixing of dark photons and Standard Model photons results in an expected interaction between dark photons and electrons, with a cross section given by⁷:

$$\sigma_{A'}(E_{A'}) = \frac{\varepsilon^2}{\beta_{A'}} \sigma_{\text{p.e.}}(E_{A'}), \quad (1)$$

where $E_{A'}$ is the dark photon's total energy, $\beta_{A'} = v_{A'}/c$ is the dark photon's relativistic beta factor, and ε is the kinetic mixing parameter.

Second, the expected cross section for the interaction of axion-like particles (ALPs) with electrons is given by^{8,9}:

$$\sigma_a(E_a) = \sigma_{\text{p.e.}}(E_a) \frac{g_{ae}^2}{\beta_a} \frac{3E_a^2}{16\pi\alpha m_e^2 c^4} \left(1 - \frac{\beta_a^{2/3}}{3}\right), \quad (2)$$

where E_a is the ALP's total energy, $\beta_a = v_a/c$ is its relativistic beta factor, α is the fine structure constant, m_e is the mass of the electron, and g_{ae} is the axioelectric coupling of the ALP to the electrons.

Note that in both (1) and (2), the interaction rate is directly dependent on the value of $\sigma_{\text{p.e.}}$. We performed an exhaustive literature search^{10–18} for measurements of $\sigma_{\text{p.e.}}$ at low energies (< 10 eV), where silicon dark matter experiments are most competitive, but found the data to be lacking for the temperature regime of interest (< 5 K). Although previous dark matter search experiments have attempted to account for the temperature dependence of $\sigma_{\text{p.e.}}$ by extrapolating from the data found in the aforementioned literature search^{1,2}, discrepancies in the high temperature data have led to low temperature projections that differ by more than an order of magnitude at energies near the silicon band gap. The result is a dominating uncertainty in any experimental sensitivity curve for dark matter models that depend on $\sigma_{\text{p.e.}}$. This limitation was the motivation for the direct measurement of $\sigma_{\text{p.e.}}$ at sub-Kelvin temperatures.

II. EXPERIMENTAL SETUP

To measure $\sigma_{\text{p.e.}}$, we designed an experiment in which a monochromatic light beam was sent through several silicon “filters” with varying thicknesses. Then, by comparing the relative transmission, a value for $\sigma_{\text{p.e.}}$ was obtained, free from many of the systematics that would be present in an absolute transmission measurement.

^{a)} Electronic mail: cstanford@g.harvard.edu

^{b)} Electronic mail: cabrera@stanford.edu

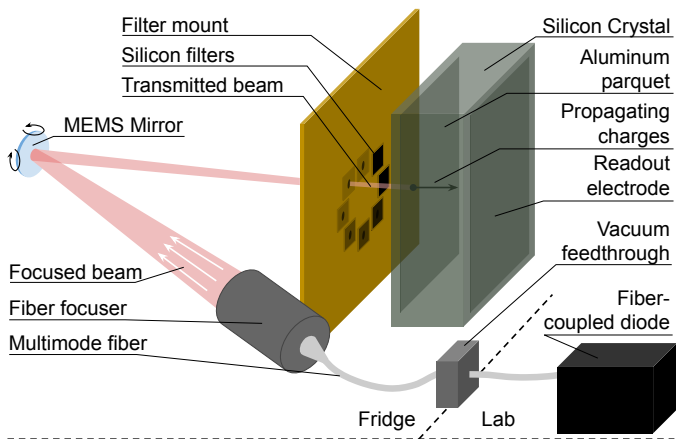


FIG. 1. The detector, which consisted of a $1\text{ cm} \times 1\text{ cm} \times 4\text{ mm}$ crystal of high purity silicon, and the laser mechanism, which used a MEMS mirror to scan a focused beam of light pulses across the back face of the crystal in order to produce a 2D image. The crystal was biased via a parquet electrode on the illuminated face.

The experiment was performed in the same ^3He cryostat used to previously measure charge propagation in silicon and germanium at low temperatures^{19–22}. The cryostat was retrofitted with a new 50/125 multi-mode fiber optic (FO) via a vacuum feed through. The FO was used to illuminate samples at the cold stage with various external light sources (LED/laser diode) of differing wavelengths (see Table I). At the base-temperature stage, the FO was directly coupled to a lens. The beam was focused to a diameter of approximately $200\ \mu\text{m}$ onto a filter mount roughly 150 mm away via a 2-axis MEMS mirror, as illustrated in Figure 1. The MEMS mirror tilt controls the x - y position of the incident beam on the filter mount, with the relaxed state set to the center of the filter mount. Thus, the angle of incidence to any radially symmetric point on the filter mount was the same.

The filter mount was made from a 6 cm^2 brass plate, illustrated in Figure 2. The front side had eight 0.5 mm diameter through-holes radially symmetric to the mount center. Adjacent holes were 2 mm apart, center-to-center. The back side had $1.6 \times 1.6\text{ mm}^2$ indents, each centered on a through-hole and used to mount a $1.5 \times 1.5\text{ mm}^2$ piece of silicon that was held in place with GE varnish. The silicon samples used in this work were cut from seven thinned, boron-doped ($\rho < 100\ \Omega\text{-cm}$) CZ Prime $\langle 100 \rangle$ wafers with thicknesses in μm of 5.1 ± 0.1 , 10.0 ± 0.1 , 24.0 ± 0.2 , 49.4 ± 0.1 , 100.2 ± 0.1 , 149.7 ± 0.2 and 198.8 ± 0.1 . One indent remained empty for calibration purposes.

Approximately 3 mm behind the filter mount (relative to the oncoming photon beam) was a silicon crystal that acted as the detector. This crystal was cut from a 4 mm -thick wafer of undoped ultra-high-purity float-zone silicon ($\sim 15\text{ k}\Omega\text{-cm}$). The residual impurity was measured to be p-type with a concentration of 10^{12} cm^{-3} . The front

Peak (nm)	LHM (nm)	UHM (nm)	Peak (eV)	Type
450	447	449	2.77	Laser
530	521	547	2.34	LED
639.5	639	640	1.94	Laser
660	651	667	1.88	LED
787	786	788	1.58	Laser
950	905	970	1.31	LED
972	970	973	1.28	Laser
1028	1027	1029	1.21	Laser

TABLE I. In order to measure the photoelectric absorption cross section over a range of energies, a series of diodes with known wavelengths was used. The transmission curves provided by the manufacturer are summarized in the peak, lower half-max (LHM), and upper half-max (UHM) columns. They were controlled with a Thorlabs DC2200 LED Driver.

(facing the oncoming beam) and back faces of the crystal were $1\text{ cm} \times 1\text{ cm}$. The front face was patterned with an aluminum-tungsten mesh electrode, with 20% coverage²³, which was used to bias the crystal to 50 V cm^{-1} . The back face was covered almost fully with an aluminum thin film that served as a ground electrode.

The silicon filters were individually illuminated with photons of different wavelengths by manipulating the MEMS mirror. The transmission through the silicon filters was measured as a charge signal in the silicon crystal detector. The charge was collected externally through an amplifier circuit by the data acquisition system (DAQ).

III. PROCEDURE

The data-taking procedure was as follows. First, the fridge was set to the desired temperature, and a light source was connected to the fiber leading into the fridge. The options for light sources spanned a range of wavelengths, summarized in Table I. Then, a run was performed at that temperature and wavelength. A run involved a scan of the beam spot over each hole, with each scan involving a 14-by-14 grid of individual measurements. To make a single measurement, the diode was pulsed in a train of 32 pulses using a Thorlabs DC2200 LED Driver. The pulses had widths of $20\ \mu\text{s}$ (some diodes required longer widths), spaced 8 ms apart. These pulses travelled down the fiber, out the focuser, and bounced off the MEMS mirror, which directed them through one of the holes in the filter mount. Then, some of the light from each pulse reflected off the silicon filter present in that hole, while another fraction of the light was absorbed by the filter. The remaining fraction was transmitted through the filter and detected.

To ensure proper alignment between the beam spot and the center of each hole, first a rough x - y value for each hole center was estimated, then a 14-by-14 grid of x - y positions was made for each hole, covering a 0.6 mm -by- 0.6 mm area surrounding that hole's estimated cen-

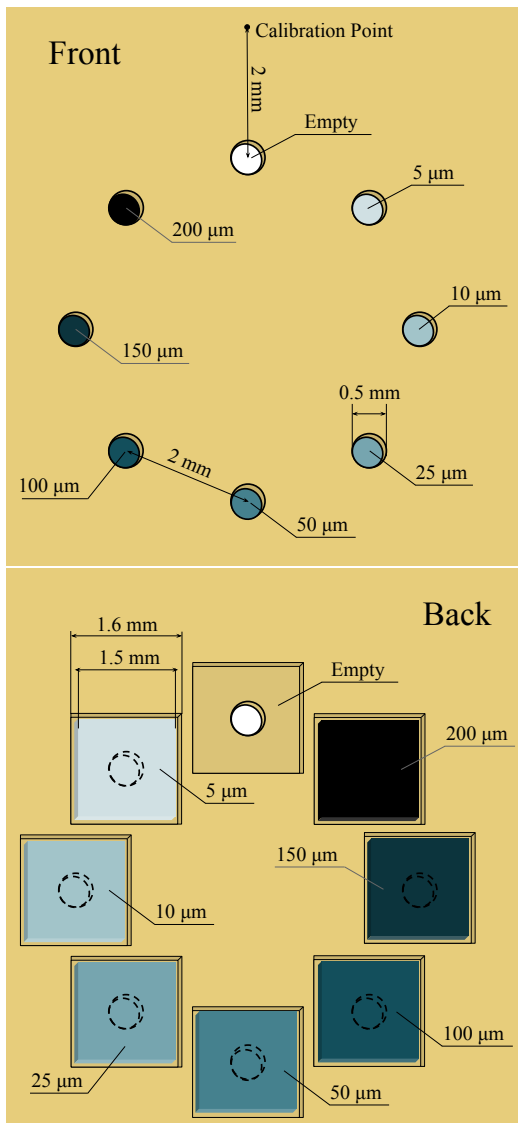


FIG. 2. **Top:** The front (facing the beam) of the filter mount featured 8 holes arrayed in a circular pattern. When the mirror was at rest, the beam spot fell in the center of the circle. This was done so that the angle of incidence of the beam at each hole (and therefore the amount of reflected light) was the same. At a distance 2 mm radially outward from the empty hole, a calibration point was designated to measure spillover light from the beam spot into neighboring holes. **Bottom:** The back (facing the detector crystal) of the filter mount featured square indents aligned with each hole, which held pieces of silicon with different thicknesses. Each piece of silicon was held in place using two small spots of GE varnish at opposing corners.

ter. Measurements were then taken at each point in these grids, in order that the maximum values for the charge collection, corresponding to precise alignment of the beam spot with a hole, could be used for the analysis.

Furthermore, to eliminate any temporal effects from biasing the results (such as a small increase in fridge temperature over the course of the run), rather than perform-

ing the scan over each hole one after another in sequence, the x-y points from all the separate scans were combined and shuffled, so that the order of measurements favored no hole in particular.

To reduce the effect of charge buildup in the crystal over time, the crystal was grounded between every measurement. While grounded, the mirror was used to direct the beam spot toward the open hole, and a 1 ms flash of light was sent into the crystal to aid in the neutralization of the charge buildup. Then, the voltage was reapplied to the crystal so the next measurement could be taken.

IV. CALIBRATION

Since each measurement involved a train of 32 light pulses, each voltage trace recorded by the DAQ was split into 32 sections and summed together to form an average pulse. The amplitude of the average pulse was used as measure of the total amount of light transmitted through the silicon and collected by the crystal during that measurement.

In order to compare two different pulse amplitudes, an absolute calibration of the detector response was needed. This was done in two steps. First, a diode was connected to the system, and the mirror directed the beam spot toward the open hole. Then, a sweep over applied current to the diode was performed, and the average pulse size at each value of the applied current was observed and recorded. Second, the same diode was placed in a dark box with a photomultiplier tube capable of counting single photoelectrons. Using the same sweep over applied current as before, an absolute measure of the crystal response to a given amount of light was obtained. What was found was that the crystal responds linearly with incident light up until average voltage pulses of 2 V, after which it begins to saturate. In the majority of runs, the width of the laser pulses was tuned so that the pulse sizes remained within this linear range, but in some cases the average pulse amplitude extended outside this range, and the absolute calibration was used to correct that amplitude.

The average amplitudes from all the measurements in each scan were then used to produce a 2-D image of that scan, to visually confirm that the scan was in fact aligned with a hole. The set of scan images for one of the runs can be seen in Figure 3, where a decrease in amplitude is seen as the the thickness of silicon increases.

V. ANALYSIS

To turn a set of scans into a value for the photoelectric absorption cross section, a series of post-processing steps was performed.

First, the set of 14-by-14 points for each scan was divided into thirds based on time of acquisition, representing the first third of points taken for that scan, the sec-

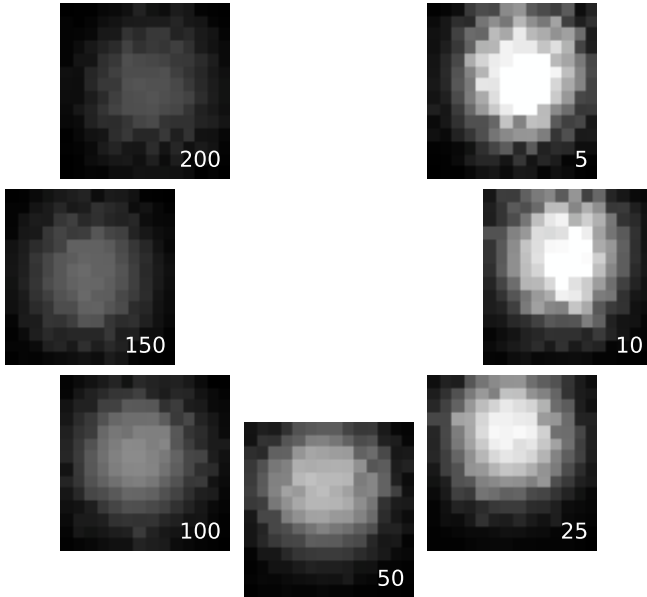


FIG. 3. A run using the 950 nm diode at 0.5 K. The run involved a scan over each hole containing a silicon filter. Each scan involved a set of 14-by-14 measurements so that the values corresponding to a precise alignment of the beam spot and the hole could be used for the analysis. The white text indicates the thickness of the silicon filter (in μm) corresponding to each scan.

ond third, and the final third. Since the points for all the scans were taken in a random order, this process effectively separated each scan into 3 “sub-scans” of lower resolution.

Second, in order to reduce the impact of outliers, the median of the top 5 amplitudes for each sub-scan was taken as the transmission value for that sub-scan. Finally, these three sub-scan transmission values were taken together, and the median of those values was taken as the transmission value for the whole scan. This reduced the impact of any transient effects at the start of a run that were present in only the first sub-scan.

Once these transmission values were obtained, they were plotted against the corresponding silicon thickness. The results from several runs taken at 0.5 K are shown in Figure 4 (Top). Note that some runs include more points than others. This is because the shorter wavelength light used for some of the runs could not be detected through the thicker pieces of silicon.

The error bars for these points were the result of a detailed study, which checked for biases introduced by various effects, such as bias voltage, light intensity, linearity correction, neutralization procedure, and day-to-day variability. However, due to the symmetric nature of the data-taking process, these were all found to be sub-dominant to the primary source of error, which was caused by the filter mount itself. This was determined by performing a calibration run where each hole of the

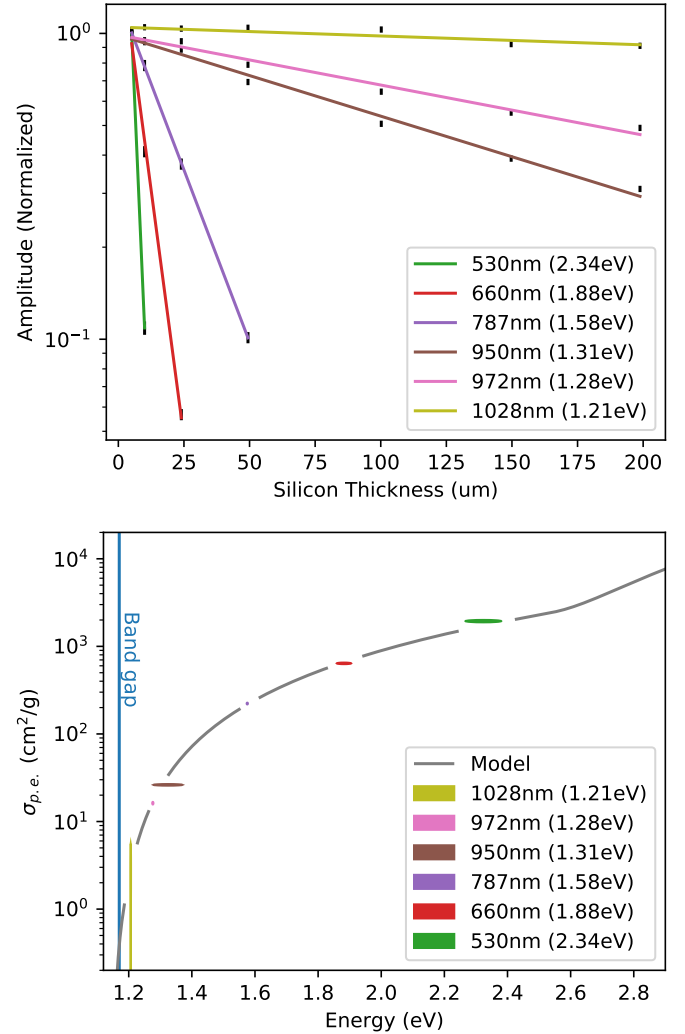


FIG. 4. **Top:** The normalized transmission through the different thicknesses of silicon for multiple wavelengths of light at 0.5 K. The error bars are dominated by systematic errors introduced by the filter mount. The negative of each fitted slope gives the value of the photoelectric absorption cross section at the corresponding wavelength. **Bottom:** The values of $\sigma_{\text{p.e.}}$ at 0.5 K from above, plotted in energy space. Each fitted value is presented as an ellipse, with the height representing the uncertainty of the fit and the width representing the uncertainty in the diode wavelength.

filter mount was left empty. The standard deviation in the light collection through the eight holes in this case was measured to be approximately 3%, with a small dependence on wavelength. A run with another mount produced by the same machining process resulted in a different variation from hole to hole, but with the same overall magnitude of variation. Since this was the dominant source of error, the standard deviation of light collection found in this calibration run was used to set the error bars in Figure 4 (Top).

After plotting, the points were fit with an exponential

according to the Beer-Lambert Law:

$$Ae^{-\rho\sigma_{p.e.}x} \quad (3)$$

where A (arbitrary constant) and $\sigma_{p.e.}$ are fit parameters, ρ is the density of silicon (2.33 g cm^{-3}), and x is the silicon thickness.

These fitted values for $\sigma_{p.e.}$ at 0.5 K are shown in Figure 4 (Bottom). Each fitted value is presented as an ellipse, with the height representing the statistical uncertainty in the fit, and the width representing the uncertainty of the diode energy. For the energy uncertainty, the lower and upper bounds were calculated from the upper half-max wavelength and lower half-max wavelength of the emission spectrum, respectively (see Table I).

VI. TEMPERATURE DEPENDENCE

The photoelectric absorption cross section is not expected to differ significantly between 0 K and the 0.5 K results presented in this paper. However, it does increase at warmer temperatures. We confirmed this effect by repeating the 0.5 K measurements at 5 K, 77 K, and 295 K. We also performed some continuous measurements at a fixed wavelength as the fridge was warming up. These data are summarized in Figure 5. We did not measure a statistically significant difference in $\sigma_{p.e.}$ for temperatures up to 77 K, but did observe an upward trend in $\sigma_{p.e.}$ between 77 K and 295 K.

VII. APPLICABILITY TO DARK MATTER SEARCHES

To set a dark matter limit, a continuous curve in $\sigma_{p.e.}$ -energy space is preferred. To obtain this curve, we fit the discrete measurements to a model describing the temperature-dependent absorption coefficient $\alpha(T)$ via direct and indirect photon absorption²⁴:

$$\alpha(T) = \sigma_{p.e.}(T)\rho_{Si} = \sum_{i,j=1,2} C_i A_j \left[\frac{(E_\gamma - E_{gj}(T) + E_{pi})^2}{e^{E_{pi}/kT} - 1} + \frac{(E_\gamma - E_{gj}(T) - E_{pi})^2}{1 - e^{-E_{pi}/kT}} \right] + A_d (E_\gamma - E_{gd}(T))^{1/2} \quad (4)$$

where E_γ is the photon energy, k is the Boltzmann constant, the first and second terms in the sum describe indirect photon absorption via phonon absorption and emission, respectively, and the last term describes direct photon absorption. The suffix i refers to the two phonon energies from the transverse acoustic (TA) ($E_p = 18.27 \text{ meV}$) and transverse optical (TO) ($E_p = 57.73 \text{ meV}$) lattice waves considered, and the suffix j refers to the two different indirect band gaps E_g which may be active in phonon absorption. We did not explicitly include in the model any direct contributions from

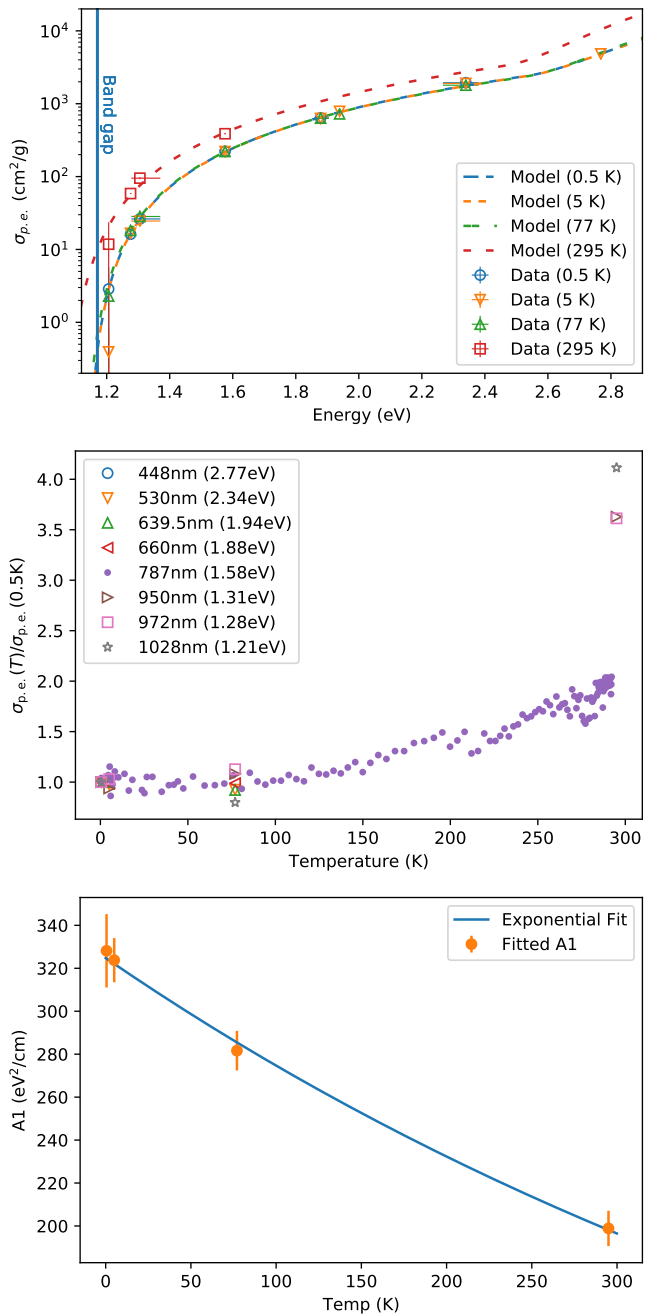


FIG. 5. **Top:** Measurements of $\sigma_{p.e.}$ at four discrete temperatures, and the results of a simultaneous fit across all four temperatures using the model described in the text. **Middle:** The temperature dependence of $\sigma_{p.e.}$ relative to $T = 0.5 \text{ K}$. The cross section for 787 nm was measured continuously as the fridge warmed up, while the cross sections for the other wavelengths were only measured at four discrete temperatures. We did not measure a statistically significant difference in the cross section for temperatures of 77 K and below. **Bottom:** When the model includes an independent parameter for the first indirect band gap proportionality constant (A_1) at each of the four measured temperatures, the fitted values follow an exponential curve.

possible B_sO_2 complexes^{25,26} in the CZ-grown silicon filters. The C_i coefficients describe the electron-phonon coupling constant; for silicon, $C_{TA} = 5.5$ and $C_{TO} = 4.0$. The A_1 , A_2 , and A_d coefficients are used as proportionality constants.

The temperature-dependent indirect band gap energies $E_{gj}(T)$ are given by:

$$E_{gj}(T) = E_{gj}(0) - \frac{\beta T^2}{T + \gamma}, \quad (5)$$

where $\beta = 7.021 \times 10^{-4} \text{ eV K}^{-1}$ and $\gamma = 1108 \text{ K}$. To improve the fit of the model to the lower energy measurements, we allowed the lowest band gap energy at 0 K ($E_{g1}(0)$) to float while using the fixed value of $E_{g2}(0) = 2.5 \text{ eV}$ for the second indirect band gap energy, where there is not enough data to constrain.

The model was fit simultaneously to the four $\sigma_{\text{p.e.}}$ measurements taken at 0.5, 5, 77, and 295 K, taking into account the uncertainties in the measured $\sigma_{\text{p.e.}}$ values as well as the uncertainties due to the diode wavelength distributions (see Table I). In this fit, $E_{g1}(0)$ was held constant across temperatures, but in order to investigate a possible temperature dependence in A_1 , we allowed A_1 to vary. Only one measurement was taken at an energy above the second indirect band gap, so the A_2 temperature dependence was not investigated.

The results of the fit for A_2 and $E_{g1}(0)$ are $6(3) \times 10^3 \text{ eV}^2 \text{ cm}^{-1}$ and $1.134(4) \text{ eV}$, respectively. The fit results for A_1 at each of the four temperatures are shown in Figure 5 (Bottom), and demonstrate a significant temperature dependence. This may be a result of temperature-dependent effects that the phenomenological absorption model described in Equation 4 does not account for, such as the effect of temperature on the density of states and the electron-phonon coupling. In order to improve the model's fit to the $\sigma_{\text{p.e.}}$ measurements and produce a result that can be used for dark matter searches, we performed a second iteration of the simultaneous fit, this time constraining A_1 to have an exponential temperature dependence:

$$A_1(T) = c_0 e^{-c_1 T}. \quad (6)$$

Using the previously determined $E_{g1}(0)$ and A_2 as fixed parameters, the fitted c_0 and c_1 values are:

$$\begin{aligned} c_0 &= 325(6) \text{ eV}^{-2} \text{ cm}^{-1} \\ c_1 &= 1.7(1) \times 10^{-3} \text{ K}^{-1}. \end{aligned} \quad (7)$$

The result of this fit is shown in Figure 5. We chose an exponential function for empirical reasons, as it was physically plausible and required few variables to adequately fit the A_1 values.

The result of this second iteration of the simultaneous fit is shown compared to the data in Figure 4 (Bottom) and Figure 5 (Top).

VIII. DISCUSSION

The requirement that the source be pulsed for this measurement restricted the light sources primarily to single-wavelength diodes, as tunable light sources are generally continuous. This limitation was largely a function of the charge amplifier, which is AC-coupled, designed for fast charge transport measurements rather than integrated power. Finer sampling of the photoelectric cross-section may be accomplished in future work by modifying the readout to accommodate a filtered xenon flash lamp (TDS) or by modifying the integrator to work with a longer time-constant tunable light source with a conventional shutter, with switching times on the scale of milliseconds.

There is an active interest in using alternative semiconductors in dark matter searches^{3,27-30}. The technique we developed can be easily extended to such materials by placing samples of that material in the filter mount. Note however that to probe the values of the cross section at photon energies below the silicon band gap, a detector crystal with a smaller gap, such as germanium, would need to be used.

IX. ACKNOWLEDGEMENTS

We would like to thank Yonit Hochberg for initial conversations that led to the design of this experiment, Brian Lenardo for his assistance with the dark box calibration, and Steve Yellin for helpful comments. This work was supported in part by the U.S. Department of Energy, the National Science Foundation, the DFG (Germany) - Project No. 420484612, and Germany's Excellence Strategy - EXC 2121 "Quantum Universe" - 390833306. The fiber feedthrough and LEDs were provided by NSERC Canada. Precision thickness measurements of the silicon filters were provided by Filmetrics (KLA) Application Lab in Santa Clara, CA. This document was prepared by using resources of the Fermi National Accelerator Laboratory (Fermilab), a U.S. Department of Energy, Office of Science, HEP User Facility. Fermilab is managed by Fermi Research Alliance, LLC (FRA), acting under Contract No. DE-AC02-07CH11359. This document was also prepared using resources of SLAC, which is operated under Contract No. DEAC02-76SF00515 with the U.S. Department of Energy.

¹R. Agnese *et al.*, Phys. Rev. Lett. **121**, 051301 (2018).

²D. W. Amaral *et al.*, "Constraints on low-mass, relic dark matter candidates from a surface-operated supercdms single-charge sensitive detector," (2020), arXiv:2005.14067 [hep-ex].

³T. Aralis *et al.* (SuperCDMS Collaboration), Phys. Rev. D **101**, 052008 (2020).

⁴A. Aguilar-Arevalo *et al.* (DAMIC Collaboration), Phys. Rev. Lett. **123**, 181802 (2019).

⁵SENSEI Collaboration, arXiv e-prints, arXiv:1901.10478 (2019), arXiv:1901.10478 [hep-ex].

- ⁶B. von Krosigk *et al.*, “Effect on dark matter exclusion limits from new silicon photoelectric absorption measurements,” Submitted for publication.
- ⁷I. M. Bloch, R. Essig, K. Tobioka, T. Volansky, and T.-T. Yu, *JHEP* **6**, 87 (2017), arXiv:1608.02123 [hep-ph].
- ⁸M. Pospelov, A. Ritz, and M. Voloshin, *Phys. Rev. D* **78**, 115012 (2008), arXiv:0807.3279 [hep-ph].
- ⁹C. Fu *et al.* (PandaX), *Phys. Rev. Lett.* **119**, 181806 (2017), arXiv:1707.07921 [hep-ex].
- ¹⁰B. Henke, E. Gullikson, and J. Davis, *Atomic Data and Nuclear Data Tables* **54**, 181 (1993).
- ¹¹M. A. Green, *Solar Energy Materials and Solar Cells* **92**, 1305 (2008).
- ¹²M. A. Green and M. J. Keevers, *Progress in Photovoltaics: Research and Applications* **3**, 189 (1995), <https://onlinelibrary.wiley.com/doi/pdf/10.1002/pip.4670030303>.
- ¹³W. C. Dash and R. Newman, *Phys. Rev.* **99**, 1151 (1955).
- ¹⁴D. F. Edwards, in *Handbook of Optical Constants of Solids*, edited by E. D. Palik (Academic Press, Burlington, 1997) pp. 547 – 569.
- ¹⁵G. G. Macfarlane, T. P. McLean, J. E. Quarrington, and V. Roberts, *Phys. Rev.* **111**, 1245 (1958).
- ¹⁶D. E. Aspnes and A. A. Studna, *Phys. Rev. B* **27**, 985 (1983).
- ¹⁷S. E. Holland, D. E. Groom, N. P. Palaio, R. J. Stover, and Mingzhi Wei, *IEEE Transactions on Electron Devices* **50**, 225 (2003).
- ¹⁸R. Hulthén, *Physica Scripta* **12**, 342 (1975).
- ¹⁹R. A. Moffatt, N. A. Kurinsky, C. Stanford, J. Allen, P. L. Brink, B. Cabrera, M. Cherry, F. Insulla, F. Ponce, K. Sundqvist, S. Yellin, J. J. Yen, and B. A. Young, *Applied Physics Letters* **114**, 032104 (2019), arXiv:1807.07986 [cond-mat.mtrl-sci].
- ²⁰C. Stanford *et al.*, *AIP Adv.* **10**, 025316 (2020), arXiv:1910.02169 [cond-mat.mtrl-sci].
- ²¹B. Shank, D. Q. Nagasawa, J. J. Yen, M. Cherry, and B. A. Young, *Journal of Low Temperature Physics* **167**, 202 (2012).
- ²²B. Shank, D. Q. Nagasawa, B. Cabrera, M. Cherry, and B. A. Young, *Journal of Low Temperature Physics* **176**, 148 (2014).
- ²³Electrode was a tri-layer of 40nm of W on 20nm of Al on 40nm of amorphous Si.
- ²⁴K. Rajakanan, R. Singh, and J. Shewchun, *Solid State Electron.* **22**, 793 (1979).
- ²⁵V. P. Markevich, M. Vaqueiro-Contreras, J. T. De Guzman, J. Coutinho, P. Santos, I. F. Crowe, M. P. Halsall, I. Hawkins, S. B. Lastovskii, L. I. Murin, and A. R. Peaker, *physica status solidi (a)* **216**, 1900315 (2019), <https://onlinelibrary.wiley.com/doi/pdf/10.1002/pssa.201900315>.
- ²⁶J. A. Hornbeck and J. R. Haynes, *Phys. Rev.* **97**, 311 (1955).
- ²⁷Y. Hochberg, Y. Kahn, M. Lisanti, K. M. Zurek, A. G. Grushin, R. Ilan, S. M. Griffin, Z.-F. Liu, S. F. Weber, and J. B. Neaton, *Physical Review D* **97** (2018), 10.1103/physrevd.97.015004.
- ²⁸S. M. Griffin, K. Inzani, T. Trickle, Z. Zhang, and K. M. Zurek, *Physical Review D* **101** (2020), 10.1103/physrevd.101.055004.
- ²⁹N. Kurinsky, T. C. Yu, Y. Hochberg, and B. Cabrera, *Physical Review D* **99** (2019), 10.1103/physrevd.99.123005.
- ³⁰S. M. Griffin, Y. Hochberg, K. Inzani, N. Kurinsky, T. Lin, and T. C. Yu, “SiC Detectors for Sub-GeV Dark Matter,” (2020), arXiv:2008.08560 [hep-ph].